

## Article

# Conceptual Model of Permafrost Degradation in an Inuit Archaeological Context (Dog Island, Labrador): A Geophysical Approach

Rachel Labrie <sup>1,\*</sup> , Najat Bhiry <sup>1</sup> , Dominique Todisco <sup>2</sup> , Cécile Finco <sup>3</sup> and Armelle Couillet <sup>4</sup> 

<sup>1</sup> Department of Geography, Centre for Northern Studies (CEN), Université Laval, Québec, QC G1V 0A6, Canada; najat.bhiry@cen.ulaval.ca

<sup>2</sup> IDEES-UMR 6266, CNRS, Department of Geography, Université de Rouen Normandie, 76130 Mont-Saint-Aignan, France; dominique.todisco@univ-rouen.fr

<sup>3</sup> Cerema, ENDSUM, 76120 Le Grand-Quevilly, France; cecile.finco@cerema.fr

<sup>4</sup> IDEES-UMR 6266, CNRS, Université de Rouen Normandie, 76130 Mont-Saint-Aignan, France; armelle.couillet@cnrs.fr

\* Correspondence: rachel.labrie.1@ulaval.ca

**Abstract:** Characterizing permafrost is crucial for understanding the fate of arctic and subarctic archaeological archives under climate change. The loss of bio-physical integrity of archaeological sites in northern regions is still poorly documented, even though discontinuous permafrost is particularly vulnerable to global warming. In this study, we documented the spatial distribution of the permafrost-supported Inuit archaeological site Oakes Bay 1 on Dog Island (Labrador, Canada) while employing a novel approach in northern geoarchaeology based on non-invasive geophysical methods. ERT and GPR were successfully used to estimate active layer thickness and image permafrost spatial variability and characteristics. The results made it possible to reconstruct a conceptual model of the current geocryological context of the subsurface in relation to the site topography, hydrology, and geomorphology. The peripheral walls of Inuit semi-subterranean sod houses were found to contain ice-rich permafrost, whereas their central depressions were identified as sources of vertical permafrost degradation. The geophysical investigations were used to classify the permafrost at Oakes Bay 1 as climate-driven, ecosystem-protected permafrost that cannot regenerate under current climate conditions. This work highlights how the permafrost at Oakes Bay 1 is currently affected by multi-point thermal degradation by both conduction and advection, which makes it highly sensitive to climate warming.

**Keywords:** permafrost; geophysics; climate change; archaeology; geoarchaeology; cultural heritage; GPR; ERT



**Citation:** Labrie, R.; Bhiry, N.; Todisco, D.; Finco, C.; Couillet, A. Conceptual Model of Permafrost Degradation in an Inuit Archaeological Context (Dog Island, Labrador): A Geophysical Approach. *Geosciences* **2024**, *14*, 95. <https://doi.org/10.3390/geosciences14040095>

Academic Editors: Fedor Lisetskii and Jesus Martinez-Frias

Received: 28 January 2024

Revised: 16 March 2024

Accepted: 20 March 2024

Published: 27 March 2024



**Copyright:** © 2024 by the authors. Licensee MDPI, Basel, Switzerland. This article is an open access article distributed under the terms and conditions of the Creative Commons Attribution (CC BY) license (<https://creativecommons.org/licenses/by/4.0/>).

## 1. Introduction

Arctic and subarctic regions have warmed at a rate of more than twice the global average since the 1980s [1]. Climate change greatly affects northern environments, and the threat it poses continues to grow. Rising air temperatures, permafrost thaw, fluctuations in precipitation, and rising sea levels affect geosystems [2] and cause physical and chemical damage to cultural heritage [3]. This looming threat poses a challenge for archaeologists and communities, as time is of the essence to locate and study these at-risk sites. However, very little is known about the impact of permafrost thaw on cultural heritage [4]. By deepening the active layer and weakening the soil supporting archaeological sites, permafrost degradation can lead to site erosion and alteration and consequently to the loss of integrity of cultural archives and historical records. This phenomenon has already been observed in some subarctic coastal areas [3,5]. Coastal erosion also has a significant impact in northern regions due to rapidly rising sea levels [6–8]. Additionally, climate change

promotes an observable increase in vegetation—also called greening or shrubification [9,10]. This phenomenon, exacerbated by permafrost thaw, causes organic artifacts to be degraded by root action and bacterial processes [3].

As most northern archaeological sites are situated in remote coastal areas, the characterization of the spatial variability of permafrost will allow us to estimate the lifespan of cultural records that are at risk of disappearing before being documented [11].

To date, only archaeological and geoarchaeological approaches have been used to provide data on the condition of northern archaeological sites and their contents. However, while these approaches are effective, they have the disadvantage of requiring a great deal of time and financial resources. They are also invasive due to the need for excavation and sampling. By contrast, geophysical methods are non-invasive and can provide data on stratigraphy and substrate conditions, complementing the standard archaeological and geoarchaeological approaches [12,13].

Geophysical methods provide a new way to study the permafrost characteristics of archaeological sites. Furthermore, the use of multiple geophysical methods provides a complete and contextual view of the study area [14–18]. Saintenoy et al. [17] used ERT and GPR in Russia to study the spatial variability in active layer depths in an area under the thermal influence of a river. Hubbard et al. [15] used a combination of LiDAR, ERT, GPR, and EMI to successfully determine subsurface hydrogeochemical/thermal zonation in relation to the surface microtopography of a coastal plain in Alaska. Geophysical methods have also been used to study northern archaeological sites, focusing on the detection of archaeological structures, artifacts, and ecofacts [19–23]. Although these studies highlight the impact of permafrost thaw on artifact preservation, they were not primarily aimed at characterizing the permafrost underlying archaeological sites. To our knowledge, a geophysics approach has never been used in northeastern Canada to document permafrost conditions at archaeological sites.

As few of the thousands of inventoried northern archaeological sites have been investigated, it is paramount to gather information on the conditions of studied sites. Models are indispensable for forecasting the future effects of climate change on permafrost and on archaeological sites that currently benefit from the presence of permafrost [3]. However, northern geoarchaeological models of all types (conceptual and numerical) are sparse. The objective of the present study is to use a multi-method geophysical approach to propose a simplified conceptual model of current geocryological conditions in relation to the geomorphology and microtopography of a vulnerable northern coastal archaeological site, not unlike many found in the north.

The study site is located on Dog Island, one of the largest islands of the Nain archipelago located in Central-North Labrador (Canada) (Figure 1). The island is in a transition zone between the Low Arctic and Subarctic climate zones, and the region is part of the discontinuous permafrost zone. Rapid warming has been observed in Labrador since the 2000s [24], particularly in the winter [25]. In accordance with this warming trend, many studies [26–29] have detected signs of permafrost thaw at the study site, but the spatial variability of permafrost is still unknown.

Key transects and zones were chosen at the Oakes Bay 1 archaeological site on Dog Island, Labrador, to conduct geophysical investigations. Ground-penetrating radar (GPR) and electrical resistivity tomography (ERT) profiles were thus generated, alongside the creation of an electromagnetic induction (EMI) map. Photogrammetric images were also obtained on-site to obtain elevation data and high-quality images of topographic features. The locations of the geophysical transects were selected according to significant changes in the topography of the archaeological site, based on the hypothesis that the permafrost table would be lower in the center of the semi-subterranean houses and would follow a degradation gradient from the coast to the interior.



**Figure 1.** Localization of Oakes Bay 1 site on Dog Island, Labrador, Canada.

## 2. Study Site

Dog Island is located approximately 35 km northeast of Nain. The region's climate is affected by the cold Labrador Current that flows southward [30] and is therefore subject to high inter-annual and intra-annual climate variability and extreme weather events. The mean annual air temperature (MAAT) is  $-2.2\text{ }^{\circ}\text{C}$ . Precipitation, half of which falls as snow during the winter months, averages 925 mm per year [31]. The periglacial conditions in the region are suitable for discontinuous permafrost due to the long period of frost (mid-September to mid-June). Tundra vegetation dominates the island, including shrubs, mosses, lichens, and some black spruce trees, several of which are in the form of krummholz. A warming trend in air temperatures has been observed in the Nain region for the past 20 years. From 1987 to 2016, winter temperatures saw a strong increase of over  $1.5\text{ }^{\circ}\text{C}/100$  years, whereas summer temperatures increased by about  $0.5\text{ }^{\circ}\text{C}/100$  years [25,32].

Dog Island (Figure 1) is part of the Nain geological province of Labrador, which consists mostly of anorthosite, granite, and gneiss from the Archean and Proterozoic eons [33]. The landscape of the Nain region is marked by the Wisconsinan glaciation and subsequent deglaciation. The Labrador segment of the Laurentide Ice Sheet covered the region until ca. 9 ka cal. yr BP [34]. Following glacial retreat (ca. 8.5 yr BP), the marine transgression reached a relative sea level of 70 m in elevation [35]. Subsequent postglacial isostatic rebound and marine regression led to the formation of several marine terraces on the islands and along the coast.

Oakes Bay is sheltered from the wind and has an abundance of marine and terrestrial resources, making it a desirable site for human occupation [26]. Thule and Inuit inhabitants established their winter settlements on a raised Holocene marine terrace on the bay's north shore at the end of the 17th century and the start of the 18th century, with the last occupation of the site dating from 1772 [36].

This period of human occupation corresponds to the Oakes Bay 1 site (Parngnertok) (Borden code: HeCg-08) (Figure 1). The site includes seven semi-subterranean sod houses and is bounded to the north by the Alagaiai mountain, to the west and east by thermokarst gullies, and to the south by a small retreating cliff facing the bay (Figure 2) [28,29]. The site was built on marine terrace T13 (T1 being the oldest terrace and T14 the most recent [27]), dated at ca. 3.5 ka cal. yr BP [35]. The terrace is 6 m above sea level. It is a paludified terrace mainly composed of silty to coarse sand, topped with peat. The dwellings consist of depressions 1 to 2 m deep and approximately 10 m in diameter that were dug into the sand of the Holocene raised beach [29]. Originally, the peripheral walls were made of peat and wood, and the floor was paved with stones. The south wall opened on a long entrance tunnel pointing toward the bay, still visible today. To the east of the tunnel of each house (on the left-hand side when exiting the house), there is a midden that is now visible as a small shrubby mound.

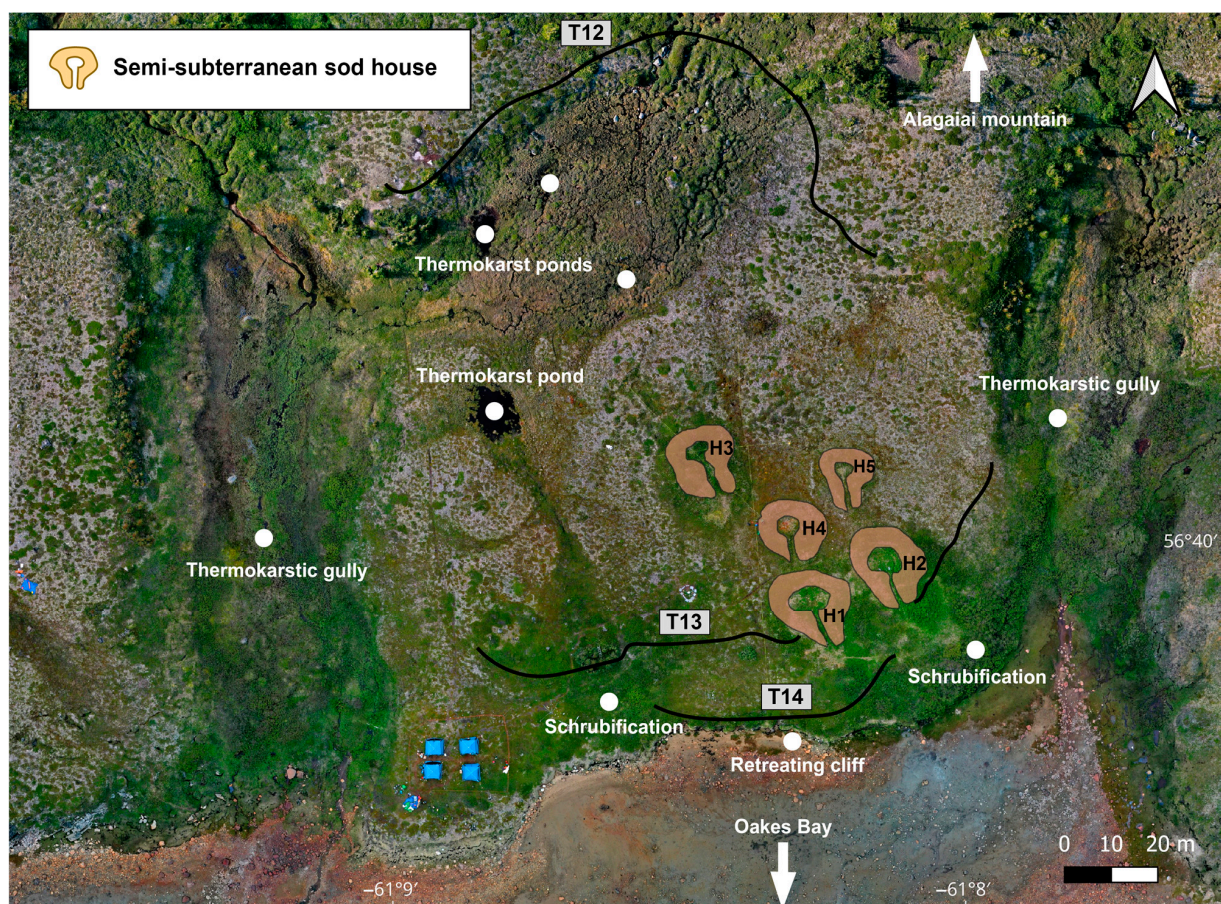


**Figure 2.** Oakes Bay 1, July 2022. Photogrammetric site image derived from 80 m elevation drone surveys. Inuit semi-subterranean sod houses are identified from H1 to H5. Marine terraces T12 to T14 are identified (T12 being the oldest and T14 the most recent).

Zones with differences in topography and plant cover were found on the study site, including thaw subsidence of permafrost mounds and thermokarst gullies and ponds. Since vegetation cover varies at the site (from bare soil to low lichens and medium shrubs), variations in permafrost conditions are also expected [37]. The intact surface of the terrace

is dominated by lichens, indicating well-drained conditions. The edges of the terrace show signs of degradation, and the coastal edge has undergone significant erosion. In low-topography areas, vegetation such as shrubs has become established. These areas include the central depression of the semi-subterranean sod houses in which snow accumulates during the winter. The subhumid conditions in these areas are also conducive to the presence of mosses, *Carex*, and other Cyperaceae (plants typically found in wetlands).

### 3. Methods

In addition to geophysical surveys, geomorphological, archaeological, and geoarchaeological data already obtained from previous studies were used. A digital surface model (DSM) [38] derived from photogrammetric information acquired by drone was also used to provide a better perspective on the microtopography's influence on the subsurface cryogenic conditions at the site. The aerial photographs were obtained using an onboard sensor (Hasselblad L1D-20c camera) on a DJI Mavic 2 Pro drone (SZ DJI Technology Co., Ltd., Shenzhen, China).

Processing of the images was performed using the Agisoft Metashape Professional application (version 1.8.3) (Table S1). Derived products (DSM and orthophotography) were georeferenced and used to study and map the site. Consequently, the locations of the electromagnetic induction (EMI), electrical resistivity tomography (ERT), and ground-penetrating radar (GPR) surveys conducted on-site in July 2022 are presented in Figure 3.

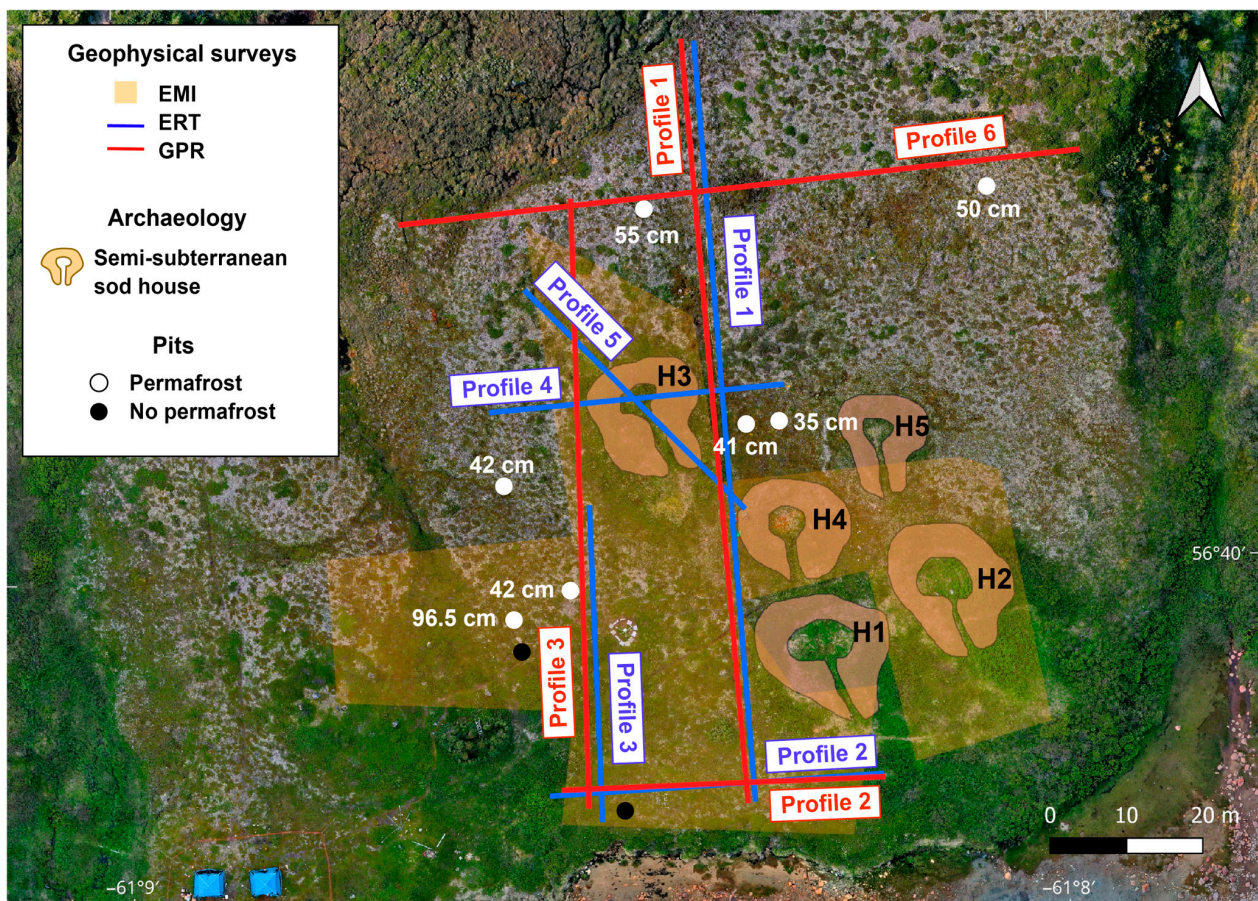


**Figure 3.** Geophysical surveys conducted on Oakes Bay 1, July 2022. Photogrammetric site image derived from 80 m elevation drone surveys. Note the shared profile names between ERT and GPR. Profile 1, Profile 2, and Profile 3 were investigated using both ERT and GPR. The depth (e.g., 42 cm) of the permafrost table as revealed by test pits is indicated. Inuit semi-subterranean sod houses are identified from H1 to H5.

### 3.1. Electrical Resistivity Tomography (ERT)

ERT is used to reconstruct the electrical resistivity of the subsurface, which is tied to ground properties. Data were acquired using the Lippmann Earth resistivity meter 4-point light 10 W, with a Wenner–Schlumberger array. This array is moderately sensitive to both horizontal and vertical structures, allowing horizontal and vertical spatial variabilities of the subsurface to be detected. It also generally has a high signal-to-noise ratio, giving reliably good-quality data [39]. Different profile lengths were investigated, ranging from 19.5 m (40 electrodes) to 100 m (80 electrodes, using the roll-on method), for a total of 5 profiles. A 0.5 m electrode spacing was used on all profiles to obtain a sufficient resolution of the upper layers of the subsurface, as the permafrost table was found to be less than 50 cm in several test pits (Figure 3). At times, salt water had to be poured on the ground to facilitate electrode coupling.

Raw data from ERT acquisitions provide information on the apparent resistivity of the substrate. The Pygimli Python library [40] was used for the inversion of the data with the DSM topography. A geophysical inversion is an iterative process used to find an electrical resistivity model that fits the field measurements (apparent resistivity) and is geologically reasonable. To assess the fit between the measured apparent resistivity and the simulated model at each iteration of the inversion process, the root mean square (RMS) error was calculated. For each profile, the inversion was carried out until the RMS error value was smaller than 5%.

Depending on the characteristics of the substrate, permafrost electrical resistivity can vary from a few thousand to millions of  $\Omega\text{m}$  [14,41]. Different types of frozen ground can therefore be identified based on electrical resistivity measurements. Ground truth from test pits was used to set a specific resistivity corresponding to permafrost. As in other studies [42–44], values of 10 k $\Omega\text{m}$  or greater were interpreted as an indication of permafrost.

The scientific literature shows that the ERT method can differentiate unfrozen from frozen ground [18,45,46]. In these highly resistive environments, the penetration depth decreases because of the screening effect: high-resistivity layers screen the current from deeper layers. In conjunction with the decrease in resolution with depth inherent to all geophysical investigation methods [47], the screening effect makes it difficult to assess the bottom of the permafrost table. As used in the present study, a depth of investigation index (DOI)-related mask of the data prevents the over-interpretation or misinterpretation of the inversion results of electrical resistivity [41].

### 3.2. Ground-Penetrating Radar (GPR)

The interface between thawed and frozen ground is known to present a strong signal on GPR radargrams due to the contrast in dielectric permittivity between the two layers [48]. Permafrost has been known to have a dielectric constant ranging between 3 and 4, whereas humid sandy soil (as found in the active layer of test pits) typically has a dielectric constant between 15 and 30 [49]. Based on this contrast, GPR was used to detect permafrost spatial variability and the top of the permafrost table. It was also used to estimate the thickness of the active layer. GPR data were collected at the study site along 4 transects, using the MALÅ EL Pro WideRange HDR with both 160 MHz and 670 MHz antennas. The use of two antennas allows for both high-surface-resolution radargrams (670 MHz frequency) and radargrams with greater penetration depth (160 MHz) for all profiles. Two W-E parallel transects (40 m and 90 m long) and two N-S parallel transects (80 m and 100 m long) were established. A differential GNSS (Global Navigation System) was used in conjunction with the radar so that geographical coordinates were associated with the radargram data. Processing of the data with Reflexw (version 9.5.7) [50] included zero-time adjustment, bandpass filtering, background noise removal, gain filtering, and conversion of travel time to depth. To ensure consistency between the representation of the same profiles acquired with both ERT and GPR, the topographic data used for topographic adjustment of the transects was exported from the DSM model. Since few hyperbolas were visible on the GPR

radargrams, the velocity of the radar waves could not be accurately estimated for all the visible layers. Consequently, ERT electrical resistivity data were used to infer the depth of the unfrozen–frozen interface, coupled with on-site pits [51]. This interface was identified in ERT data by the transition between conductive material to highly resistive material. The depth of this transition on ERT profiles was thus used to calibrate the depth of the linear interface visible in GPR data. This calibration gave an estimated electromagnetic wave velocity of 0.07 m/ns above the permafrost table. A velocity of 0.07 m/ns was thus used to convert the vertical axis into depth for all the profiles.

It is known that GPR is an effective and fast method for studying the subsurface. Resistive materials, such as permafrost, ground ice, sand, and gravel, provide a good medium for the propagation of electromagnetic waves [51]. A strong interface can, however, reflect great quantities of energy, masking deeper structures [52]. Radar signals are attenuated by electrically conductive materials, such as brackish or salt water, clay, and magnetic rocks. Proximity to water, particularly salt water, can therefore greatly attenuate the signal [52].

### 3.3. Electromagnetic Induction (EMI)

An electromagnetic induction survey was also conducted at the site to target potential permafrost zones that could then be investigated with ERT and GPR, as EMI may be used for fast contactless mapping of electrical conductivity. However, since the electrical conductivity of the substrate was often too low for the EMI device's sensibility (less than 1 mS/m), this approach could not be used. The measured values were indeed considered too close to the noise level. Thus, site selection and survey line design relied on the nature and magnitude of the features that were observed at the surface. Apparent electrical conductivity maps still showed qualitative conductivity trends for the zones that were inspected (Figure S1). Additional information on the method and results obtained can be found in the additional content section.

## 4. Results and Interpretation

### 4.1. On-Site Pits and Pedostratigraphy

On-site, soil pit tests were excavated down to the top of the permafrost table (bottom of the active layer). In the absence of permafrost, the maximum depth reached without frozen ground was recorded [46]. Each pit displayed some micro-lateral variability of active layer thickness, so pit interpretations represent average unit thicknesses.

Test pits revealed a podzolized soil overlaid with peat (Figure 4). The soil profile consisted of oxidized fine to medium sand with lenses of coarse sand and gravel (Bf horizon), overlain by oxidized red sand and pale gray sand (Ae horizon) and finally by peat (O horizon).

This general pedostratigraphy corresponds with the horizons provided by Roy et al. [27] in their study of the coastal side of the site. Pits were generally located less than 5 m from ERT and GPR profiles, providing reasonable accuracy on structure and stratigraphic thicknesses. However, as the depth and lateral distribution of permafrost vary along the pits, caution is needed when using the test pits as ground truth, as these differences as well as the ambiguity in pit locations relative to the geophysical profiles may cause uncertainty in depth calculations.

### 4.2. Electrical Resistivity Tomography (ERT)

The analysis of changes in the inverted electrical resistivity profiles attests to several tendencies, resulting in four units with different characteristics (Figure 5): 1. a relatively low-resistivity unit from the top of the profiles to a depth of about 1 m (U1—300  $\Omega\cdot\text{m}$  to 1000  $\Omega\cdot\text{m}$ ); 2. a moderately resistive unit (U2—1000  $\Omega\cdot\text{m}$  to 25k  $\Omega\cdot\text{m}$ ); 3. a highly resistive unit (U3—>25 k $\Omega\cdot\text{m}$ ) usually found at a depth of about 1 m; and 4. a low-resistivity unit (more conductive) (U4—<1000  $\Omega\cdot\text{m}$ ) at greater depths. To enable a comparison between the resistivities presented in the different profiles, a common color scale has been chosen

(300  $\Omega\cdot\text{m}$ –53 k $\Omega\cdot\text{m}$ ). Profile 1, Profile 4, and Profile 5 (Figure 5A,D,E) had resistivities of up to 56 k $\Omega\cdot\text{m}$ , 56 k $\Omega\cdot\text{m}$ , and 72 k $\Omega\cdot\text{m}$ , respectively.

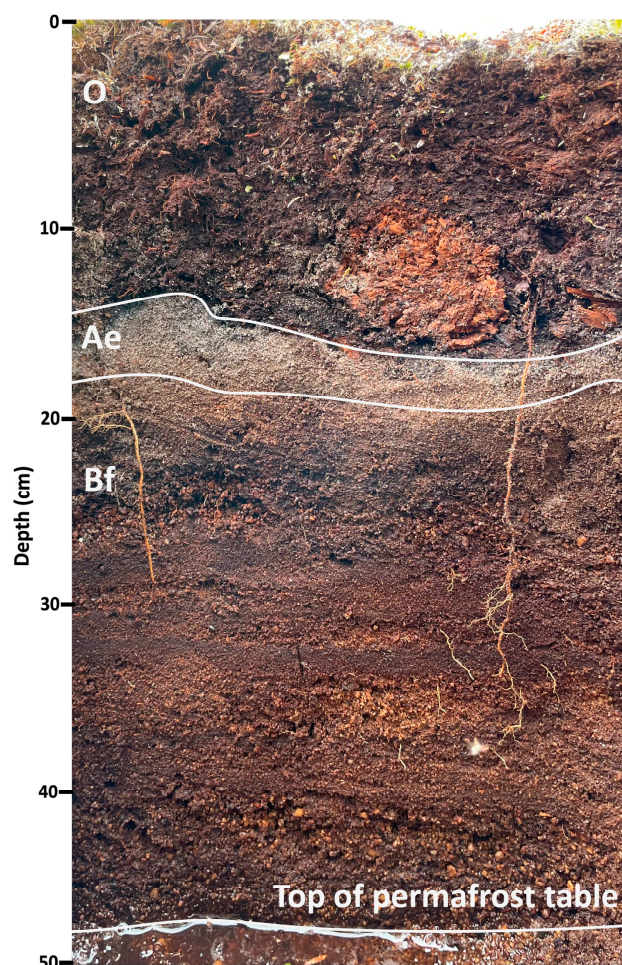


**Figure 4.** Pedostratigraphy of test pits, corresponding to a podzolized soil overlain by peat. At about 48 cm depth, ice that started to melt when exposed to air is visible (top of the permafrost table). Test pits revealed a podzolized soil composed of a dark red illuvial Bf horizon overlaid by a light-colored eluvial Ae horizon and an organic O horizon.

Unit U1 corresponds to the thawed active layer, composed of a peat layer overlying humid sand. This conductive zone's thickness ranges from 50 cm to 1 m. An abrupt transition from a few hundreds of  $\Omega\cdot\text{m}$  to thousands of  $\Omega\cdot\text{m}$  was detected between U1 and U2 (Figure 5) on all profiles. This transition between U1 and U2 is interpreted as the limit between the active layer and underlying frozen ground, which was confirmed by at least one on-site test pit. The depth of this sharp increase in resistivity depends on the terrain slope and the proximity to thermokarst features at the surface. An approximative minimum electrical resistivity value for permafrost in each profile was determined and later used for the calibration of the GPR interfaces. U2 presents resistivities ranging from a few thousand  $\Omega\cdot\text{m}$  up to 25k  $\Omega\cdot\text{m}$  and is therefore interpreted as frozen sand, as was confirmed by direct observations in test pits [53]. An exception can be made for the test pit near Profile 2, where no permafrost was found even though a U2 zone was identified on the profile. This can be explained by the distance between the profile and the test pit, as the latter was 3 m closer to the coast. This underscores the high variability in permafrost distribution at the site, even on a small scale.

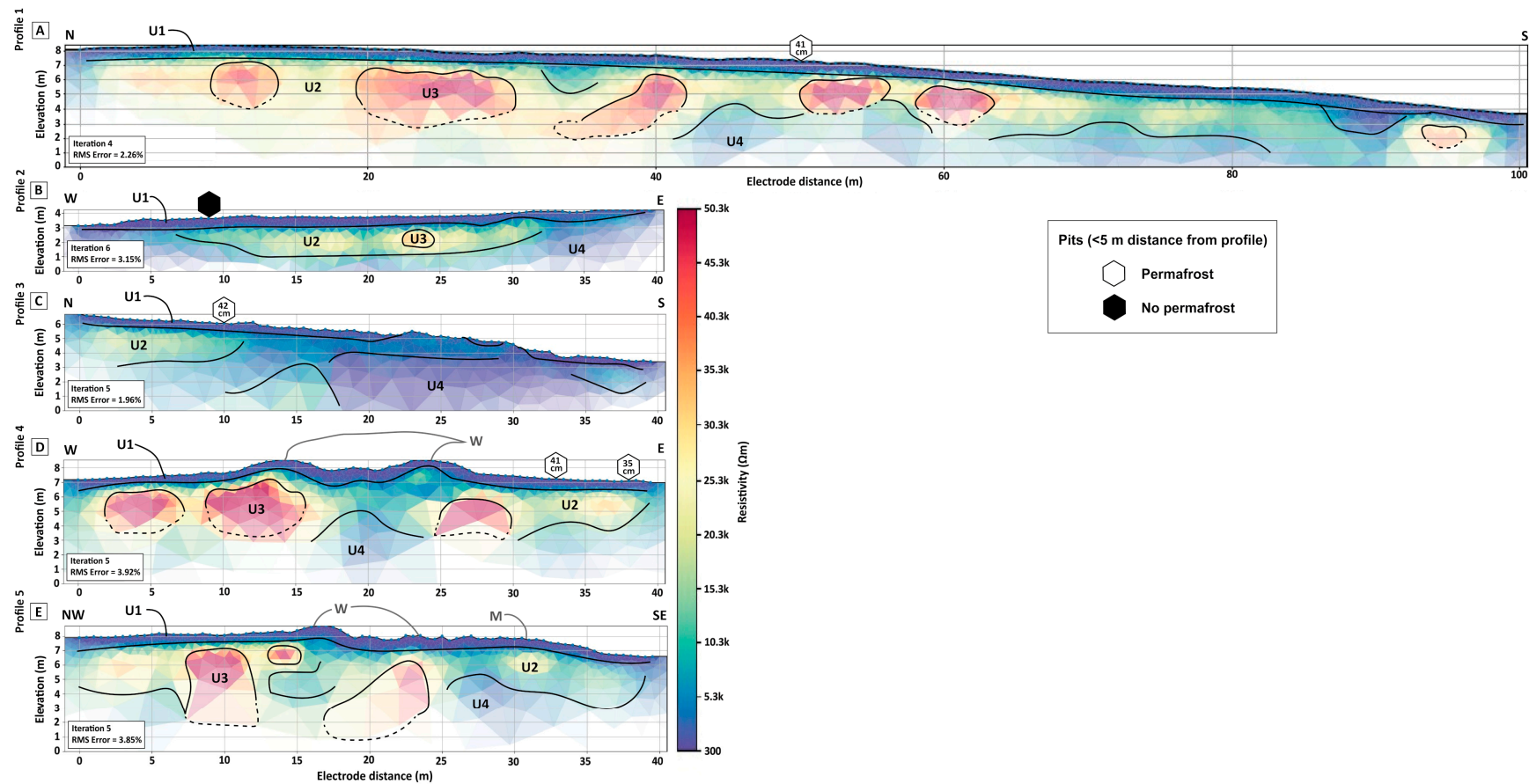


**Figure 5.** Electrical resistivity tomography (ERT) profiles and positions of permafrost and ice-rich permafrost along the profiles. (A) Profile 1 (N-S). (B) Profile 2 (W-E). (C) Profile 3 (N-S). (D) Profile 4 crossing the semi-subterranean sod house H3 (W-E). (E) Profile 5 crossing the semi-subterranean sod house H3 (NW-SE). Vertical elevation scale varies for the different profiles. Resistivity scale is the same for all ERT profiles. RMS Error: Root Mean Square error in percent. Contours indicate features interpreted from the surveys (U1: active layer; U2: permafrost; U3: ice-rich permafrost; U4: unfrozen soil or talik). Grey W and M designate the walls of semi-subterranean sod house H3 and its midden, respectively. Whiten (masked) area corresponds to zones with low data resolution. Test pits located < 5 m from the profiles are shown, with the depth of the top of the permafrost table indicated.

U3 is a highly resistive unit ( $U3 \rightarrow >25 \text{ k}\Omega\cdot\text{m}$ ) found beneath U1. The vertical and horizontal extent of unit U3 is heterogeneous from profile to profile and inside each profile. The very-high-resistivity zones in Profiles 1, 4, and 5 (Figure 5A,D,E) could indicate a high ground-ice content in the sediments, or massive ice. Massive ice has been known to have resistivity values ranging from  $10\text{k } \Omega\cdot\text{m}$  to  $40\text{k } \Omega\cdot\text{m}$  and more [53,54], but its presence could only be confirmed by drilling. Some profiles had no resolution beneath U3, which can be due to the umbrella effect of highly resistive permafrost. Indeed, some zones and depths under highly resistive structures cannot be assessed with electrical measurements from the surface [41,55]. In Profile 1 (Figure 5A), a thickness gradient of unit U3 from inland (north) to the coast (south) is present; residual highly resistive zones become thinner when located closer to the coast. A comparison of the thickness of U3 between Profile 2 (Figure 5B) and Profiles 4 and 5 (Figure 5D,E) also illustrates this gradient. U3 is absent in the central depression of house H3, and the lower-resistivity zones U1 and U2 expand downwards (Figure 6). This can be explained by the insulation from the cold being provided by snow accumulation in the depression during the winter. Profile 5 (Figure 5E) presented a U3 zone between 20 and 25 m, where the electrodes were planted in the midden of house H3. The high resistivity in this zone could be due to the presence of frozen sediments, frozen cultural material (faunal remains, charcoal, etc.) [29], or buried resistant materials.

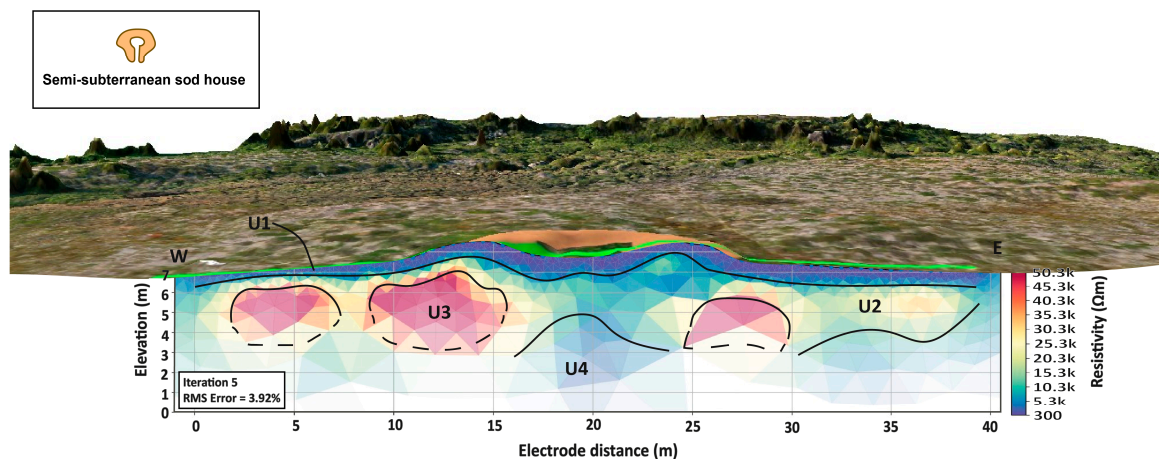


**Figure 6.** Electrical resistivity tomography (ERT) Profile 4 crossing the semi-subterranean sod house H3 (W-E). Absolute error: RMS error. Contours indicate features interpreted from the surveys (U1: active layer; U2: permafrost; U3: ice-rich permafrost; U4: unfrozen soil or talik). The whitened area corresponds to zones with low data resolution. The walls of the house contain ice-rich permafrost, whereas its topographically depressed center induces permafrost degradation by snow accumulation in the winter.

Unit U4 has resistivity values similar to U1, indicating the absence of permafrost (Figure 5). The conductive zone of U4 is interpreted as being either taliks or the water table. Here, taliks refer to regions of perennially unfrozen ground surrounded by permafrost bodies, as well as regions in proximity to permafrost bodies (Figure 5C). Taliks can be due to a local anomaly in thermal, hydrological, or hydrochemical conditions [56]. Electrical resistivity is generally lower in a water-saturated substrate [14]. The electrical resistivities of U4 therefore are consistent with wet/unfrozen sediment. As highlighted earlier, caution must be used when interpreting this unit, as the highly resistive U3 unit may shield the actual electrical resistivity of those deeper zones. However, U4 zones not overlain by highly resistive permafrost, such as between 20 and 40 m of Profile 3 (Figure 5C), offer a better resolution and can be interpreted with greater confidence. These low-resistivity zones correlate with the presence of taller and denser surface vegetation like shrubs, as in the center of the semi-subterranean sod house H3 (Figure 5D,E) and the low-topography zones on the extremities of Profile 2 (Figure 5B). The U4 zone of Profile 3 is more extended than

in the other profiles (Figure 5C). This could be explained by its proximity to a zone of thermokarst gullying, and therefore a thermal and hydrological anomaly.

The heterogeneity of thickness and resistivity values from the ERT profiles indicates that the characteristics of the subsurface may vary over small distances, even if only over a few meters. The electrical resistivity of frozen soil depends on unfrozen water content, soil temperature, soil type and texture, and soil salinity [14]. Therefore, the resistivity at which the ground is considered frozen may vary from profile to profile. This is to be expected, as the study site is in a zone of discontinuous and dispersed permafrost [57].

#### 4.3. Ground-Penetrating Radar (GPR)

Four main units were identified and interpreted in the 160 MHz radargrams (Figure 7): 1. a unit from the top of the profiles to a depth of about 1 m, composed of many linear reflectors underlain by a clear interface (U1); 2. an unattenuated unit underneath the clear interface at the bottom of U1, or faint signal multitudes (U2); 3. a unit of strong signal multitudes (U3); and 4. a unit of highly attenuated signal (U4) at greater depths and near humid zones. These units are classified by their radargram characteristics and correspond to the units identified by ERT. The 160 MHz radargrams were used to identify permafrost characteristics, as this frequency allows more penetration depth beyond the top of the permafrost table.

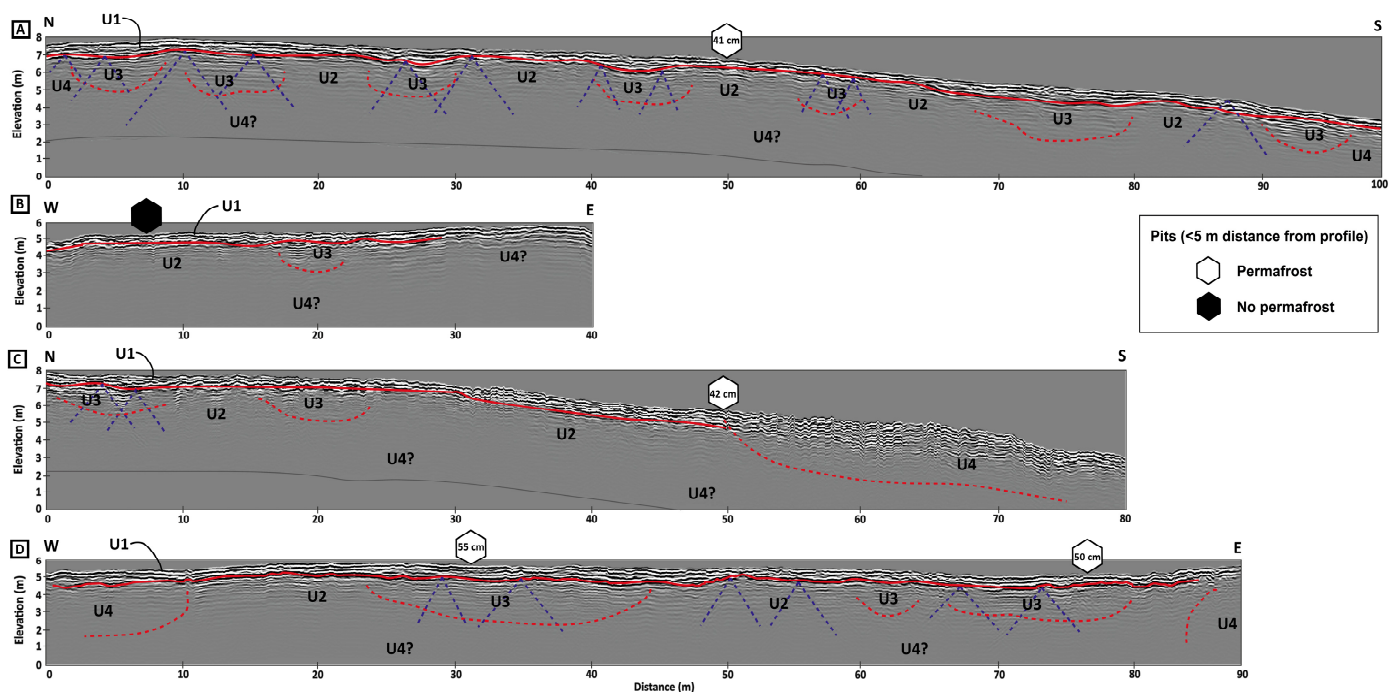


**Figure 7.** Ground-penetrating radar (GPR) profiles at a frequency of 160 MHz. (A) Profile 1 (N-S). (B) Profile 2 (W-E). (C) Profile 3 (N-S). (D) Profile 6 (W-E). Maximum elevation varies for the different profiles. Contours indicate features interpreted from the radargrams (U1: active layer; U2: permafrost; U3: ice-rich permafrost; U4: unfrozen soil or talik). The red continuous line corresponds to the bottom of the active layer. The dashed red line identifies the zonation of the units, and the dashed blue line identifies hyperbolas from possible ice wedges. For Profiles (A,C), the sea is located about 7 m to the south of each profile's south extremity. Test pits located < 5 m from the profiles are shown, with the depth of the top of the permafrost table indicated.

The interface at the bottom of U1 (at a depth of 1 m) (Figure 8) has a shape close to the topography and could be an indicator of the bottom of the active layer [58]. Furthermore, this strong interface indicates a high contrast of relative dielectric permittivity, which could

indicate the contrast between frozen and unfrozen sediments [53,59]. Accordingly, this interface was identified as the bottom of the active layer (top of the permafrost table).

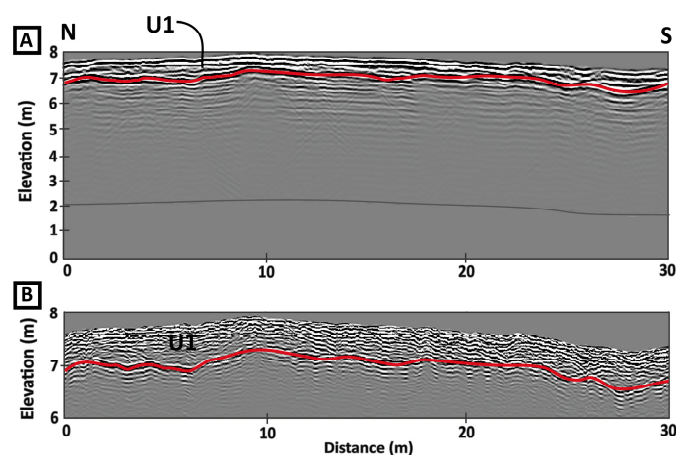


**Figure 8.** Interface interpreted as the transition between unfrozen and frozen soil. Both radargrams correspond to the first 30 m of GPR Profile 1. (A) Radargram at 160 MHz frequency. (B) Radargram at 670 MHz frequency. The red line corresponds to the bottom of the active layer. The stratigraphy of the active layer is visible as linear reflectors in U1. Note the vertical scale difference between boxes (A,B).

In all the profiles, linear reflectors in the thawed active layer (U1) correspond to the sandy stratified sediments confirmed by test pit findings (Figure 8). Figure 8B presents a 670 MHz radargram from Profile 1, cropped at a distance of 30 m to visualize the many interfaces imaged in the active layer.

Linear dipping reflectors were found at depths between 50 and 80 m on Profile 3, in unit U4 (Figure 7C). As these reflectors follow the shape of surface topography, they were identified as layers of unfrozen sediment overlain by peat. GPR has been known to successfully detect the interface between peat and silt in the active layer [59]. Due to the high resistivity of U3, radar waves are reflected on this ice-rich layer and therefore detail the layers within the active layer. The many visible layers are consistent with the pedostratigraphy identified in the test pits (Figure 4), which showed sediments with variable grain size. The characteristic pattern of peat on a radargram is of planar bedding [60], which was observed at the east end of Profile 3 (Figure 7C).

U3 is a zone that shows strong multiples of the permafrost table reflector (Figure 7). These multiples result from the resonance of the linear reflector at the bottom of U1 (Figure 8), which suggests a strong contrast in the dielectric properties of the materials. According to previous studies [54,61], a zone where multiples of the reflector are visible may correspond to ice-rich frozen sediment or massive ice. Due to the relative homogeneity of ground ice, few reflections other than the resonance of the previous interface were visible [60]. Profiles 1, 3, and 6 (Figure 7A,C,D) show hyperbola reflectors that could be associated with ice wedges. Indeed, GPR is known to detect ice wedges [62–64], as ice wedges act as point sources that induce hyperbolic reflections [62] because of the contrast in electrical permittivity between the massive ice and surrounding permafrost. The head of the visible hyperbolas would correspond to the top of the ice wedges. They would therefore be located at the base of the active layer. Ice wedge depth would correspond to the hyperbolic reflections caused by the base of the wedge [65]. Those hyperbolic reflectors are not visible in the zones near water or thermokarst, as in Profile 2 and the last 30–80 m of Profile 3 (Figure 7). These findings reinforce the probability that these reflectors indicate ice wedges, as they seem to be present only in profiles with dry and cold conditions. Moreover, Foury [29] has noted the presence of ice wedges measuring about 20 cm long inside the midden of the semi-subterranean sod house H1 on the site. However, no polygonal network

was visible at the surface. This may be because the ice wedges appear to be positioned beneath the active layer, rendering their pattern invisible at the surface.

For Profiles 2 and 6 (Figure 7B,D), signal attenuation at the beginning and end of the profiles is associated with proximity to humid zones, such as thermokarst ponds, that have high electrical conductivity. U4 zones can therefore be interpreted as taliks.

A maximum penetration with a good resolution of about 3 m in depth was attained for all profiles at 160 MHz (Figure 7). For the 670 MHz antenna, the signal penetrated to a maximum of about 2 m (Figure 8B). As the more electrically conductive the medium, the more the radar signal is attenuated, this attenuation of the signal may be caused by unfrozen wet sediment (U4) or the presence of more fine-grained sediment. In support of this interpretation, Roy et al. [27] showed the presence of silty sand at a depth of about 2 m through stratigraphic cross-sections. The attenuation of the signal may also be the result of the strong dielectric contrast between the active layer and resistive permafrost, preventing the radar wave from penetrating deeper [53,60,66]. Due to this signal attenuation, bedrock depth cannot be determined.

## 5. Discussion

### 5.1. Complementarity of the Geophysical Methods

ERT and GPR were used to identify four units within the subsurface (Table 1). These were identified as follows: U1—active layer; U2—permafrost; U3—ice-rich permafrost; U4—talik or water table. Possible ice wedges identified by GPR were mostly found in U3 zones (Figure 6), with some also found in U2 zones (Figure 7D). Both methods identified taliks (U4) in proximity to thermokarst (Figure 5; Figure 7).

**Table 1.** Units identified by ERT and GPR based on their characteristics.

Unit	Description	ERT Characteristics	GPR Characteristics
U1	Active layer	300 $\Omega\cdot\text{m}$ to 1000 $\Omega\cdot\text{m}$	Many linear reflectors underlain by clear interface
U2	Permafrost	Thousands of $\Omega\cdot\text{m}$	Unattenuated zone underneath clear interface
U3	Ice-rich permafrost	>25 $\text{k}\Omega\cdot\text{m}$	Signal multiples
U4	Talik or water table	<1000 $\Omega\cdot\text{m}$	Highly attenuated signal

The combination of ERT and GPR results demonstrates that the use of both methods can provide information about the geocryological conditions of the site. Their combined use made it possible to interpret those data in ways that would not have been feasible when relying solely on either one of the two datasets. The use of GPR alone could not have permitted the identification of ice-rich permafrost zones (U3), as signal multiples occur because of very high contrast in dielectric permittivity (which could be the contrast between frozen–unfrozen sediment, or vice versa). The comparison with ERT data made it possible to identify ice-rich permafrost zones, as they correlate with areas of high electrical resistivity. This interpretation was in part confirmed through on-site test pits. However, probing would be required to verify the presence of ice deeper in the subsurface, as test pits only attained the top of the permafrost layer. Figure 9 shows the superimposed ERT and GPR data and interpretation for Profile 1.

Both ERT and GPR data identified the top of the permafrost table with confidence, as the thawed active layer provided a strong contrast with the frozen soil. Using the 670 MHz antenna for GPR allowed us to image the interior of the active layer and detail stratigraphy (Figure 8). Both ERT and GPR (160 MHz) provided an investigation depth of 3–4 m, below which resolution was lost. By combining those two methods, the relationship between surface features and the subsurface was made clearer.

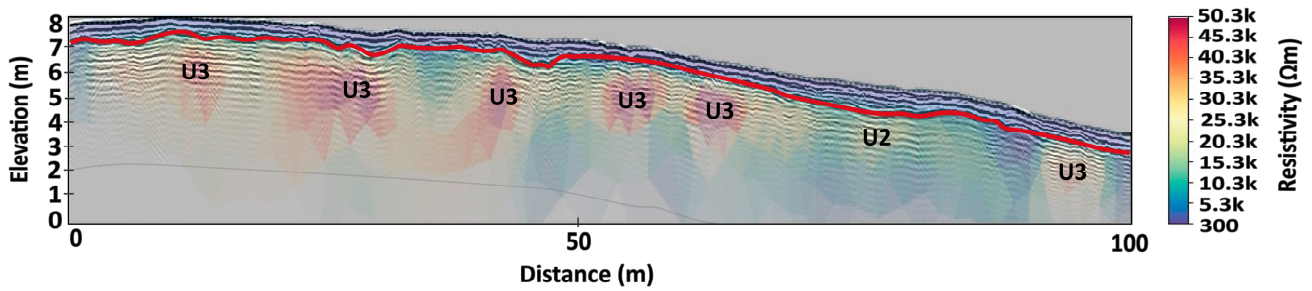


**Figure 9.** Correspondence of superimposed ERT and GPR data for Profile 1. The red line corresponds to the bottom of the active layer as seen by a continuous linear reflector in GPR data. This interface corresponds to the transition between high conductivity ( $300 \Omega\cdot\text{m}$ ) and high resistivity ( $10 \text{ k}\Omega\cdot\text{m}$  and more) in ERT data. Zones of high amplitude reflector multiples in GPR data correspond to zones of high electrical resistivity in ERT data (U3). Both datasets were topographically corrected using microtopography derived from photogrammetry.

5.2. Current Distribution of Permafrost at the Site Scale

The comparison of data obtained using GPR and ERT provides valuable insights into the geocryological context of the Oakes Bay 1 site. The information obtained is summarized in the conceptual model presented in Figure 10.

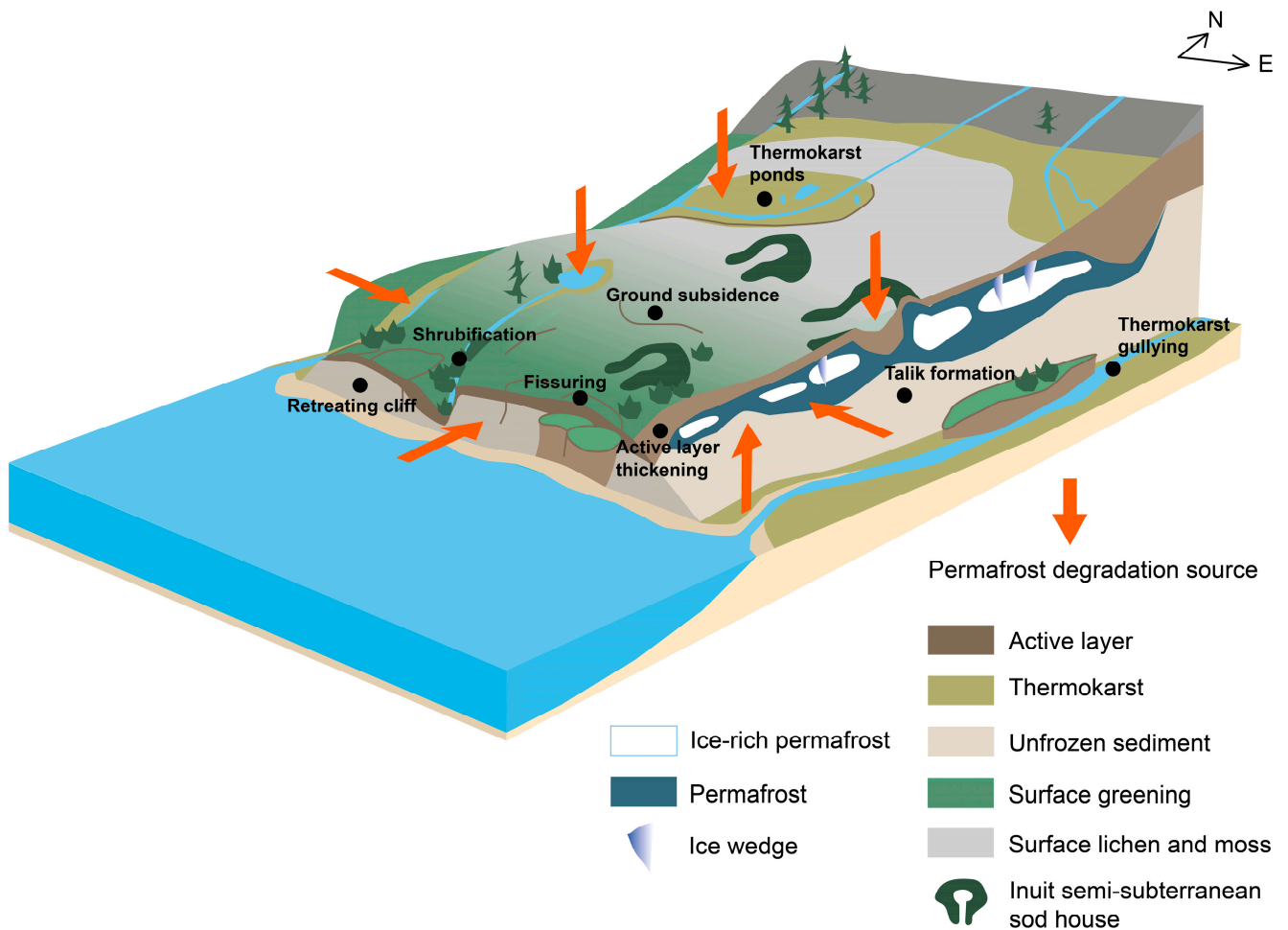


**Figure 10.** Conceptual model of current geocryological conditions at Oakes Bay 1 in relation to surface features and processes. Vertical and lateral degradation threatens permafrost.

Massive ice has been known to occur mainly in continental locations, but massive ice landforms (peat plateaus, palsas, ice wedges, etc.) have also been documented in coastal locations in Canada [8,67–69]. While the presence of massive ice has been underestimated by large-scale studies on the Labrador coast, field-based studies and many inhabitants of Inuit communities have noted its presence [70]. Ice-rich permafrost has also been observed at depths of 3 to 4 m in Nain, 35 km west of the study site [71]. Differences in sediment grain size influence the formation of ground ice: thicker ice lenses can form in fine-grained sediments, and thinner ice lenses form in coarser sediments [72]. As Oakes Bay 1 is mainly composed of sand and silty sand, it is extremely unlikely that there could be a massive ice body at the site. Instead, the frozen structures that were identified likely correspond to sand with a high segregated ice content, as is common in water-saturated sandy sediments, or are indicative of ice wedges. The high ground-ice content of the site is supported by research carried out by Roy et al. [27], which proposed that the paludification (peat formation due to the transition from mesic to wet conditions) of the terrace 13 of Oakes Bay 1 was caused by the impermeabilization of the ground due to permafrost formation. This finding also correlates with the location of the possible ice wedges, at the bottom of the active layer and therefore inactive and buried. The ice wedges would have grown with an epigenetic process. Furthermore, thaw subsidence caused by thermokarst gullying to the west and east of the site (Figure 10) suggests that there once was excess ice in the now unfrozen soil [18].

In addition to the detection of the bottom of the active layer, ERT and GPR data revealed the homogeneous presence of a 50 cm–1 m thick active layer over the entirety of the site. As the measurements were made in July, active layer thickness would have been near its annual maximum [73]. Most of the profiles showed the presence of frozen sediment underlying the active layer, except for the south end of Profile 3, which indicated a zone interpreted as a talik. This finding could be explained by the proximity of this zone to a highly shrubby topographic depression with overland flow (Figure 11).

ERT and GPR profiles reveal a permafrost thickness of at least a few meters. This, however, represents an approximation, as the highly resistive frozen ground did not allow the identification of the permafrost's base. Thinner permafrost is located near topographic depressions and thermokarst ponds.

As shown in Figure 10, the permafrost at Oakes Bay 1 is currently affected by multi-point thermal degradation due to a combination of the following factors: unfrozen sediments deep in the subsurface, contact with the sea, the well-insulated interior of the semi-subterranean sod houses, and already existing thermokarst features. The site is affected by two heat-transfer mechanisms: conduction and advection [74]. The movement of water along the coastal cliff interacting with the sea and within thermokarst ravines primarily accelerates permafrost degradation through advection mechanisms. The central depression of the semi-subterranean sod houses on the other hand contributes to permafrost degradation mainly through conduction mechanisms. Permafrost can also thaw from its base due to geothermal heat conducted from the Earth's core [74].

The contact with seawater induces thermo-erosion of coastal permafrost, as seawater causes degradation both laterally and from below, creating a horizontal “permafrost wedge” affected both by air temperature degradation from above and seawater temperature degradation from below [75,76]. This also induces a positive feedback loop, as ice-free sediments are looser and less resistant to coastal erosion and gullying.

### 5.3. Current Distribution of Permafrost within Inuit Semi-Subterranean Sod Houses

Spatial and thermal variations in permafrost are a direct consequence of interactions between climate and climate-driven elements such as vegetation, snow cover, peat thickness, and ground-ice content [46,77]. At the site level, microtopography drives the lateral redistribution of snow, liquid water, and vegetation, which in turn modify the ground's thermal and hydrological regime [78,79]. The spatial variations of permafrost in the subsurface are therefore closely linked to microtopography.

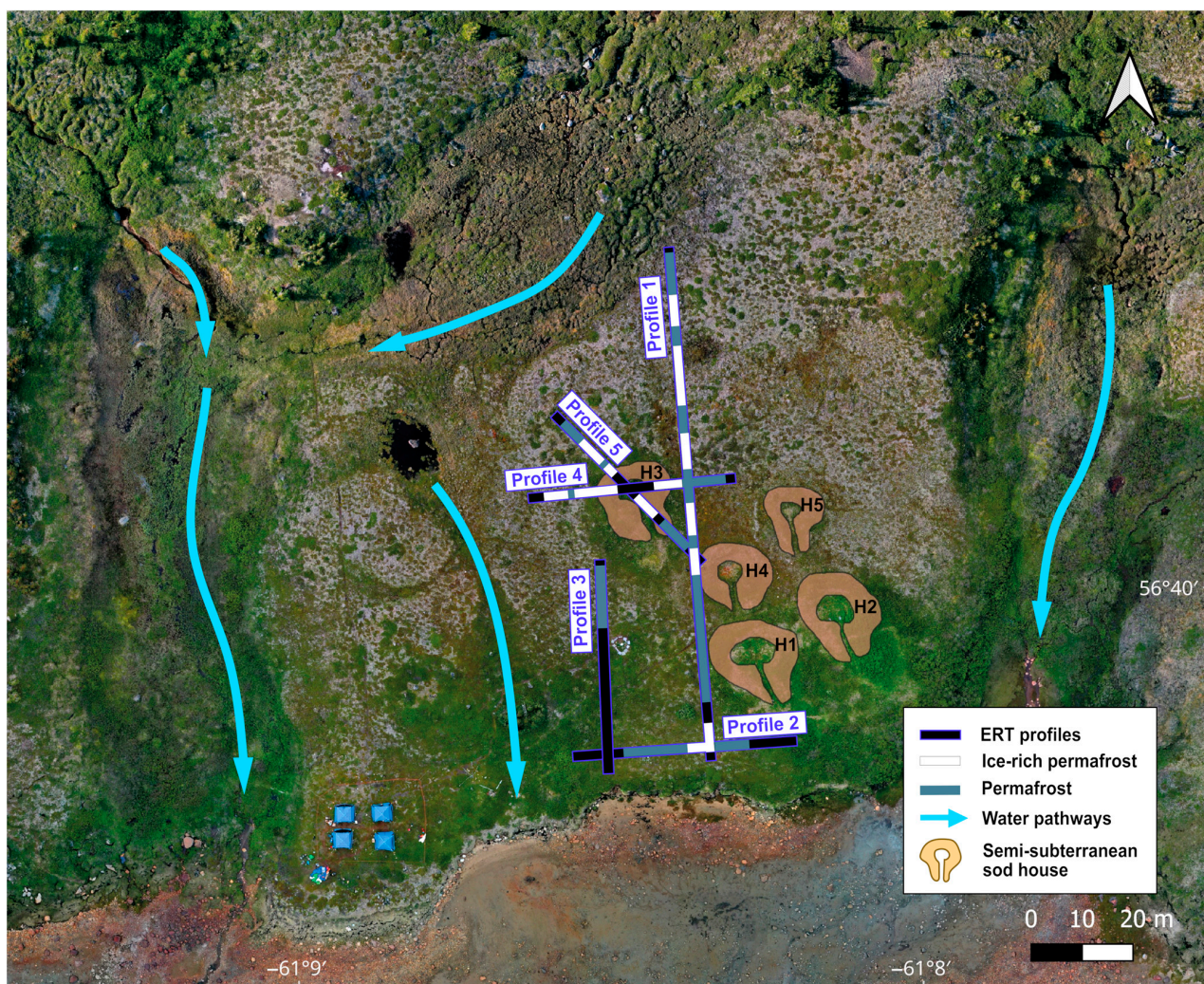


**Figure 11.** Permafrost and ice-rich permafrost along the ERT profiles in relation to surface features and water pathways.

This relationship is evident in the distribution of permafrost in the semi-subterranean houses. The elevated peripheral walls provide significant exposure to cold temperatures and therefore contain ice-rich permafrost in the subsurface (Figure 6). By contrast, the central depressions of the houses contribute to active layer thickening, shrubification, and permafrost thaw, as they trap snow that insulates the ground from cold (Figure 6). Permafrost degradation therefore occurs by conduction from the surface. Some of the semi-subterranean houses are also located close to the shore of Oakes Bay (1–2 m) (Figure 2) and are thus threatened by coastal erosion and seawater thermo-erosion.

#### 5.4. Anticipated Evolution of Permafrost at Oakes Bay 1

Field geophysical studies and the resulting conceptual model allow us to classify the current discontinuous permafrost in Oakes Bay as a climate-driven, ecosystem-protected permafrost [80]. This corresponds to permafrost that has grown under favorable postglacial climatic conditions and is maintained during warmer conditions by being protected by the ecosystem and soil properties. The possible presence of inactive ice wedges buried under the current active layer, as suggested by GPR results, further reinforces this classification. This type of discontinuous permafrost is particularly sensitive to anomalies in climatic, thermal, hydrological, and hydrochemical conditions [81]. Once degraded, it will not be able to re-establish itself under present climatic conditions [80]. Relatively thin ice-rich permafrost such as that found at Oakes Bay 1 is even more sensitive to climatic changes [82].

Air temperatures in the region are projected to warm significantly during the 21st century, with the largest warming (+6.7 °C) occurring after 2050 [25]. This warming would significantly increase surface runoff, active layer thickening, and coastal erosion caused by a higher sea level. Sea level rise also greatly impacts permafrost by thawing the frozen ground both laterally and vertically [83]. Hydrological changes will therefore greatly influence the distribution of permafrost at the Oakes Bay 1 site. As it is thawing, ice-rich permafrost causes ground subsidence and produces thermokarst ponds. The present-day topography and geomorphology of the site provide evidence that its long-term evolution is governed by lateral thermokarst and coastal erosion, and by thermokarst processes on the raised terrace itself, where pond formation has started.

Permafrost properties are also highly dependent on the nature of the vegetation cover [37]. The freezing front generally penetrates deeper in places dominated by lichens and low shrubs than in places dominated by medium shrubs or trees [84]. It is thus to be expected that as the current warming trend continues, the shrubification of the site will be amplified, along with thaw subsidence.

## 6. Conclusions

In this study, with the use of a novel approach in northern geoarchaeology, the geocryological context of a subarctic coastal archaeological site was studied for the first time in northeastern Canada. The characterization of the frozen ground supporting the Oakes Bay 1 archaeological site provides a valuable case study for many other coastal northern archaeological sites that face similar climatic and geomorphological pressures. The results show that geophysical methods can provide an overview of the spatial variability of permafrost in relation to surface features. ERT and GPR were successfully used to estimate the thickness of the active layer and the spatial heterogeneity of frozen ground. These geophysical methods confirmed the impact of topography and hydrology on the distribution of frozen ground and confirmed the classification of the permafrost at Oakes Bay 1 as climate-driven, ecosystem-protected permafrost that cannot regenerate under current climate conditions. The peripheral walls of the Inuit semi-subterranean sod houses were found to contain ice-rich permafrost, whereas the central depressions of the houses were identified as sources of vertical permafrost degradation. The results produced by the three geophysical methods were, however, affected by the site's high resistivity: the penetration depth of ERT and GPR was reduced, and EMI electrical conductivity measurements were too low for the resolution of the device. Because the electrical conductivity measurements from the EMI device were too close to noise levels, we did not consider these data in this study. Indeed, the apparent conductivity of the zone reveals that the terrain is very resistant to electricity, probably because of the presence of ground ice [52]. For soils with coarse sediments and the possibility of high ground-ice content, the EMI method would thus not be recommended.

Documenting the distribution of permafrost provides a firm foundation for making projections about the future degradation of similar coastal archaeological sites in the north. Historically, the cold subarctic conditions facilitated the preservation of archaeological material and structures. However, future temperature warming will increasingly endanger this cultural heritage [3]. In addition, shrubification induced by a warming climate also causes physical damage to organic archaeological artifacts, as roots penetrate the soil. Roots may also disturb the archaeological context or artifacts, rendering site interpretation even more difficult [85].

While the physical site may deteriorate and ultimately be lost, preservation can still be accomplished through collaborative means [86]. The model presented in this study may be regarded as a starting point for efforts to document and contextualize this Inuit cultural heritage site. By assessing the physical condition of Oakes Bay 1, an alternative future for the site may be achieved in collaboration with the Nain community. The present study also represents an instructive case study on the importance of the management of high-latitude sites that contain archaeological information threatened by the effects of climate change.

**Supplementary Materials:** The following supporting information can be downloaded at <https://www.mdpi.com/article/10.3390/geosciences14040095/s1>: Figure S1: Map of apparent electrical conductivity at a depth of 1.1 m as measured by electromagnetic induction (EMI); Table S1: Methodology for acquiring and processing images obtained by onboard sensors.

**Author Contributions:** R.L.: investigation, formal analysis, software, visualization, writing—original draft preparation; N.B.: investigation, project administration, conceptualization, funding acquisition, supervision, writing—review and editing; D.T.: investigation, conceptualization, resources, supervision, writing—review and editing; C.F.: investigation, methodology, validation, software, writing—review and editing. A.C.: investigation, software. All authors have read and agreed to the published version of the manuscript.

**Funding:** This research was funded by the Natural Sciences and Engineering Research Council of Canada (NSERC) grant number RGPIN-2020-06699 as well as the Agence nationale de la recherche (ANR), Inter-Arctic project (ANR-17-CE3-0009), 2018-23 program. Logistic and material support was provided by the Centre d'études nordiques (CEN), Université Laval. The internship at IDEES laboratory (Université de Rouen, France) was in part funded by Sentinel North's internship scholarship program.

**Data Availability Statement:** Data are contained within the article or Supplementary Material.

**Acknowledgments:** This work is the result of an ongoing collaboration between the Nunatsiavut government, the community of Nain, and Université Laval. We thank the Nain community for its involvement and interest in the present research project and its logistical support for fieldwork. We thank the Webb family for its collaboration, as well as Rodney Merkuratsuk for his help in the fieldwork. Thanks are extended to Yann Rantier for fieldwork drone acquisitions, and we are grateful to Luis Henrique Cavalcante Fraga for aid in geophysical data treatments. Thanks to Louise Marcoux for her help in cartographic representation. We express our profound gratitude to James Woollett, respected archaeologist and zooarchaeologist at Laval University, for his crucial role in overseeing the diligent execution of all fieldwork conducted during the summers of 2018, 2019, 2021 and 2022. His invaluable contributions and discussions greatly enriched our research endeavors. We thank the Centre d'études nordiques (CEN) for its logistical support (Université Laval), as well as Sentinel North. We extend thanks to the reviewers of this manuscript.

**Conflicts of Interest:** The authors declare no conflicts of interest. The funders had no role in the design of the study; in the collection, analyses, or interpretation of data; in the writing of the manuscript; or in the decision to publish the results.

## References

1. Wilson, S. *AMAP Assessment 2016: Chemicals of Emerging Arctic Concern*; Arctic Monitoring and Assessment Programme (AMAP): Oslo, Norway, 2017; ISBN 978-82-7971-104-9.
2. Hassol, S.J. *Impacts of a Warming Arctic: Arctic Climate Impact Assessment*; Cambridge University Press: Cambridge, UK, 2004; ISBN 978-0-521-61778-9.
3. Hollesen, J.; Callanan, M.; Dawson, T.; Fenger-Nielsen, R.; Friesen, T.M.; Jensen, A.M.; Markham, A.; Martens, V.V.; Pitulko, V.V.; Rockman, M. Climate Change and the Deteriorating Archaeological and Environmental Archives of the Arctic. *Antiquity* **2018**, *92*, 573–586. [[CrossRef](#)]
4. Nicu, I.C.; Fatorić, S. Climate Change Impacts on Immobile Cultural Heritage in Polar Regions: A Systematic Bibliometric Review. *WIREs Clim. Chang.* **2023**, *14*, e822. [[CrossRef](#)]
5. Friesen, T.M. The Arctic CHAR Project: Climate Change Impacts on the Inuvialuit Archaeological Record. *Nouv. Archéologie* **2015**, *141*, 31–37. [[CrossRef](#)]
6. Lantuit, H.; Pollard, W.H. Fifty Years of Coastal Erosion and Retrogressive Thaw Slump Activity on Herschel Island, Southern Beaufort Sea, Yukon Territory, Canada. *Geomorphology* **2008**, *95*, 84–102. [[CrossRef](#)]
7. O'Rourke, M.J.E. Archaeological Site Vulnerability Modelling: The Influence of High Impact Storm Events on Models of Shoreline Erosion in the Western Canadian Arctic. *Open Archaeol.* **2017**, *3*, 1–16. [[CrossRef](#)]
8. Way, R.G.; Lewkowicz, A.G.; Zhang, Y. Characteristics and Fate of Isolated Permafrost Patches in Coastal Labrador, Canada. *Cryosphere* **2018**, *12*, 2667–2688. [[CrossRef](#)]
9. Tape, K.; Sturm, M.; Racine, C. The Evidence for Shrub Expansion in Northern Alaska and the Pan-Arctic. *Glob. Chang. Biol.* **2006**, *12*, 686–702. [[CrossRef](#)]
10. Myers-Smith, I.H.; Forbes, B.C.; Wilmking, M.; Hallinger, M.; Lantz, T.; Blok, D.; Tape, K.D.; Macias-Fauria, M.; Sass-Klaassen, U.; Lévesque, E.; et al. Shrub Expansion in Tundra Ecosystems: Dynamics, Impacts and Research Priorities. *Environ. Res. Lett.* **2011**, *6*, 045509. [[CrossRef](#)]

11. Fenger-Nielsen, R.; Elberling, B.; Kroon, A.; Westergaard-Nielsen, A.; Matthiesen, H.; Harmsen, H.; Madsen, C.K.; Stendel, M.; Hollesen, J. Arctic Archaeological Sites Threatened by Climate Change: A Regional Multi-threat Assessment of Sites in South-west Greenland. *Archaeometry* **2020**, *62*, 1280–1297. [[CrossRef](#)]
12. Conyers, L.B. *Ground-Penetrating Radar for Geoarchaeology*; John Wiley & Sons Inc: Hoboken, NJ, USA, 2016; ISBN 978-1-118-95000-5.
13. Siart, C.; Forbriger, M.; Bubbenzer, O. *Digital Geoarchaeology: New Techniques for Interdisciplinary Human-Environmental Research*; Natural Science in Archaeology; Springer International Publishing: Cham, Switzerland, 2018; ISBN 978-3-319-25314-5.
14. Kneisel, C.; Hauck, C.; Fortier, R.; Moorman, B. Advances in Geophysical Methods for Permafrost Investigations. *Permafrost. Periglac. Process.* **2008**, *19*, 157–178. [[CrossRef](#)]
15. Hubbard, S.S.; Gangodagamage, C.; Dafflon, B.; Wainwright, H.; Peterson, J.; Gusmeroli, A.; Ulrich, C.; Wu, Y.; Wilson, C.; Rowland, J.; et al. Quantifying and Relating Land-Surface and Subsurface Variability in Permafrost Environments Using LiDAR and Surface Geophysical Datasets. *Hydrogeol. J.* **2013**, *21*, 149–169. [[CrossRef](#)]
16. Sjöberg, Y.; Marklund, P.; Pettersson, R.; Lyon, S.W. Geophysical Mapping of Palsa Peatland Permafrost. *Cryosphere* **2015**, *9*, 465–478. [[CrossRef](#)]
17. Saintenoy, A.; Pessel, M.; Grenier, C.; Léger, E.; Danilov, K.; Bazhin, K.; Khristoforov, I.; Séjourné, A.; Konstantinov, P. Coupling GPR and ERT Data Interpretation to Study the Thermal Imprint of a River in Syrdakh (Central Yakutia, Russia). In Proceedings of the 18th International Conference on Ground Penetrating Radar, Golden, CO, USA, 14–19 June 2020; Society of Exploration Geophysicists: Golden, CO, USA, 2020; pp. 93–96.
18. Bussière, L.; Schmutz, M.; Fortier, R.; Lemieux, J.; Dupuy, A. Near-surface Geophysical Imaging of a Thermokarst Pond in the Discontinuous Permafrost Zone in Nunavik (Québec), Canada. *Permafrost. Periglac. Process.* **2022**, *33*, 353–369. [[CrossRef](#)]
19. Modin, I.N.; Arzhantseva, I.A.; Andreyev, M.A.; Akulenko, S.A.; Kats, M.Y. Geophysical Investigations on Por-Bajin Island in the Republic of Tuva. *Mosc. Univ. Geol. Bull.* **2010**, *65*, 428–433. [[CrossRef](#)]
20. Wolff, C.B.; Urban, T.M. Geophysical Analysis at the Old Whaling Site, Cape Krusenstern, Alaska, Reveals the Possible Impact of Permafrost Loss on Archaeological Interpretation. *Polar Res.* **2013**, *32*, 19888. [[CrossRef](#)]
21. Hodgetts, L.; Dawson, P.; Eastaugh, E. Archaeological Magnetometry in an Arctic Setting: A Case Study from Maguse Lake, Nunavut. *J. Archaeol. Sci.* **2011**, *38*, 1754–1762. [[CrossRef](#)]
22. Landry, D.B.; Ferguson, I.J.; Milne, S.B.; Park, R.W. Combined Geophysical Approach in a Complex Arctic Archaeological Environment: A Case Study from the LdFa-1 Site, Southern Baffin Island, Nunavut. *Archaeol. Prospect.* **2015**, *22*, 157–170. [[CrossRef](#)]
23. Hodgetts, L.M.; Eastaugh, E.J.H. The Role of Magnetometry in Managing Arctic Archaeological Sites in the Face of Climate Change. *Adv. Archaeol. Pract.* **2017**, *5*, 110–124. [[CrossRef](#)]
24. Way, R.G.; Viau, A.E. Natural and Forced Air Temperature Variability in the Labrador Region of Canada during the Past Century. *Theor. Appl. Climatol.* **2015**, *121*, 413–424. [[CrossRef](#)]
25. Barrette, C.; Brown, R.; Way, R.; Mailhot, A.; Émilie, P.; Diaconescu, P.; Grenier, D.; Chaumont, D.; Dumont, C.; Sévigny, S.; et al. Chapter 2: Nunavik and Nunatsiavut regional climate information update. In *Nunavik and Nunatsiavut: From Science to Policy, an Integrated Regional Impact Study (IRIS) of Climate Change and Modernization, Second Iteration*; Ropars, P., Allard, M., LeMay, M., Eds.; ArcticNet Inc.: Québec, QC, Canada, 2020.
26. Woollett, J. Oakes Bay 1: A Preliminary Reconstruction of a Labrador Inuit Seal Hunting Economy in the Context of Climate Change. *Geogr. Tidsskr.-Dan. J. Geogr.* **2010**, *110*, 245–259. [[CrossRef](#)]
27. Roy, N.; Bhiry, N.; Woollett, J. Environmental Change and Terrestrial Resource Use by the T Hule and I Nuit of L Labrador, C Anada. *Geoarchaeology* **2012**, *27*, 18–33. [[CrossRef](#)]
28. Couture, A.; Bhiry, N.; Monette, Y.; Woollett, J. A Geochemical Analysis of 18th-Century Inuit Communal House Floors in Northern Labrador. *J. Archaeol. Sci. Rep.* **2016**, *6*, 71–81. [[CrossRef](#)]
29. Foury, Y.; Bhiry, N.; Woollett, J.; Bhiry, N.; Woollett, J. *L'occupation du Site Hivernal Inuit Oakes Bay 1 (HeCg-08), Labrador, Canada: Micromorphologie et Zooarchéologie des Dépotoirs*; Université Laval: Québec, QC, Canada, 2017.
30. Marko, J.R.; Fissel, D.B.; Wadhams, P.; Kelly, P.M.; Brown, R.D. Iceberg Severity off Eastern North America: Its Relationship to Sea Ice Variability and Climate Change. *J. Clim.* **1994**, *7*, 1335–1351. [[CrossRef](#)]
31. Données Climatiques Historiques. Available online: <https://climat.meteo.gc.ca/> (accessed on 20 December 2023).
32. Ouellet-Bernier, M.-M.; De Vernal, A.; Chartier, D.; Boucher, É. Historical Perspectives on Exceptional Climatic Years at the Labrador/Nunatsiavut Coast 1780 to 1950. *Quat. Res.* **2021**, *101*, 114–128. [[CrossRef](#)]
33. Wardle, R.J.; Gower, C.F.; Ryan, B.; Nunn, G.A.G.; James, D.T.; Kerr, A. *Geological Map of Labrador; 1:1 Million Scale*; Geological Survey, Map 97-07; Government of Newfoundland and Labrador, Department of Mines and Energy: Labrador, NL, Canada, 1997.
34. Margold, M.; Stokes, C.R.; Clark, C.D. Reconciling Records of Ice Streaming and Ice Margin Retreat to Produce a Palaeogeographic Reconstruction of the Deglaciation of the Laurentide Ice Sheet. *Quat. Sci. Rev.* **2018**, *189*, 1–30. [[CrossRef](#)]
35. Clark, P.U.; Fitzhugh, W.W. Late Deglaciation of the Central Labrador Coast and Its Implications for the Age of Glacial Lakes Naskaupi and McLean and for Prehistory. *Quat. Res.* **1990**, *34*, 296–305. [[CrossRef](#)]
36. Roy, N.; Woollett, J.; Bhiry, N.; Lemus-Lauzon, I.; Delwaide, A.; Marguerie, D. Anthropogenic and Climate Impacts on Subarctic Forests in the Nain Region, Nunatsiavut: Dendroecological and Historical Approaches. *Écoscience* **2021**, *28*, 361–376. [[CrossRef](#)]
37. Oblogov, G.E.; Vasiliev, A.A.; Streletskiy, D.A.; Shiklomanov, N.I.; Nyland, K.E. Localized Vegetation, Soil Moisture, and Ice Content Offset Permafrost Degradation under Climate Warming. *Geosciences* **2023**, *13*, 129. [[CrossRef](#)]

38. Guth, P.L.; Van Niekerk, A.; Grohmann, C.H.; Muller, J.-P.; Hawker, L.; Florinsky, I.V.; Gesch, D.; Reuter, H.I.; Herrera-Cruz, V.; Riazanoff, S.; et al. Digital Elevation Models: Terminology and Definitions. *Remote Sens.* **2021**, *13*, 3581. [[CrossRef](#)]
39. Dahlin, T.; Zhou, B. A Numerical Comparison of 2D Resistivity Imaging with 10 Electrode Arrays. *Geophys. Prospect.* **2004**, *52*, 379–398. [[CrossRef](#)]
40. Rücker, C.; Günther, T.; Wagner, F.M. pyGIMLi: An Open-Source Library for Modelling and Inversion in Geophysics. *Comput. Geosci.* **2017**, *109*, 106–123. [[CrossRef](#)]
41. Marescot, L.; Loke, M.H.; Chapellier, D.; Delaloye, R.; Lambiel, C.; Reynard, E. Assessing Reliability of 2D Resistivity Imaging in Mountain Permafrost Studies Using the Depth of Investigation Index Method. *Surf. Geophys.* **2003**, *1*, 57–67. [[CrossRef](#)]
42. Supper, R.; Ottowitz, D.; Jochum, B.; Römer, A.; Pfeiler, S.; Kauer, S.; Keuschnig, M.; Ita, A. Geoelectrical Monitoring of Frozen Ground and Permafrost in Alpine Areas: Field Studies and Considerations towards an Improved Measuring Technology. *Surf. Geophys.* **2014**, *12*, 93–115. [[CrossRef](#)]
43. Hauck, C.; Kneisel, C. *Applied Geophysics in Periglacial Environments*, 1st ed.; Cambridge University Press: Cambridge, UK, 2008; ISBN 978-0-521-88966-7.
44. Halla, C.; Blöthe, J.H.; Tapia Baldis, C.; Trombotto Liaudat, D.; Hilbich, C.; Hauck, C.; Schrott, L. Ice Content and Interannual Water Storage Changes of an Active Rock Glacier in the Dry Andes of Argentina. *Cryosphere* **2021**, *15*, 1187–1213. [[CrossRef](#)]
45. You, Y.; Yu, Q.; Pan, X.; Wang, X.; Guo, L. Application of Electrical Resistivity Tomography in Investigating Depth of Permafrost Base and Permafrost Structure in Tibetan Plateau. *Cold Reg. Sci. Technol.* **2013**, *87*, 19–26. [[CrossRef](#)]
46. Douglas, T.A.; Jorgenson, M.T.; Brown, D.R.N.; Campbell, S.W.; Hiemstra, C.A.; Saari, S.P.; Bjella, K.; Liljedahl, A.K. Degrading Permafrost Mapped with Electrical Resistivity Tomography, Airborne Imagery and LiDAR, and Seasonal Thaw Measurements. *Geophysics* **2016**, *81*, WA71–WA85. [[CrossRef](#)]
47. Urruela, A.; Rivero, L.; Casas, A.; Garcia-Artigas, R.; Sendrós, A.; Lovera, R.; Himi, M. Improving the Resolution of Investigation Using ERT Instruments with a Reduced Number of Electrodes. *J. Appl. Geophys.* **2021**, *186*, 104239. [[CrossRef](#)]
48. Everett, M.E. *Near-Surface Applied Geophysics*, 1st ed.; Cambridge University Press: Cambridge, UK, 2013; ISBN 978-1-107-01877-8.
49. Martinez, A.; Byrnes, A.P. Modeling Dielectric-Constant Values of Geologic Materials: An Aid to Ground-Penetrating Radar Data Collection and Interpretation. *Curr. Res. Earth Sci.* **2001**, *247*, 1–16. [[CrossRef](#)]
50. Sandmeier, K.J. *Reflexw-Program for the Processing of Seismic, Acoustic or Electromagnetic Reflection, Refraction and Transmission Data*, (version 9.5.7). Windows; Sandmeier Geophysical Research: Karlsruhe, Germany, 2020.
51. Campbell, S.; Affleck, R.T.; Sinclair, S. Ground-Penetrating Radar Studies of Permafrost, Periglacial, and near-Surface Geology at McMurdo Station, Antarctica. *Cold Reg. Sci. Technol.* **2018**, *148*, 38–49. [[CrossRef](#)]
52. Davis, J.L.; Annan, A.P. Ground-Penetrating Radar for High-Resolution Mapping of Soil and Rock Stratigraphy<sup>1</sup>. *Geophys. Prospect.* **1989**, *37*, 531–551. [[CrossRef](#)]
53. De Pascale, G.P.; Pollard, W.H.; Williams, K.K. Geophysical Mapping of Ground Ice Using a Combination of Capacitive Coupled Resistivity and Ground-penetrating Radar, Northwest Territories, Canada. *J. Geophys. Res. Earth Surf.* **2008**, *113*, 2006JF000585. [[CrossRef](#)]
54. Angelopoulos, M.C.; Pollard, W.H.; Couture, N.J. The Application of CCR and GPR to Characterize Ground Ice Conditions at Parsons Lake, Northwest Territories. *Cold Reg. Sci. Technol.* **2013**, *85*, 22–33. [[CrossRef](#)]
55. Hilbich, C.; Marescot, L.; Hauck, C.; Loke, M.H.; Mäusbacher, R. Applicability of Electrical Resistivity Tomography Monitoring to Coarse Blocky and Ice-rich Permafrost Landforms. *Permafr. Periglac. Process.* **2009**, *20*, 269–284. [[CrossRef](#)]
56. Harris, S.A.; French, H.M.; Heginbottom, J.A.; Johnston, G.H.; Ladanyi, B.; Sego, D.C.; van Everdingen, R.O. *Glossary of Permafrost and Related Ground-Ice Terms*; National Research Council of Canada. Associate Committee on Geotechnical Research; Permafrost Subcommittee: Ottawa, ON, Canada, 1988; 159p.
57. Lewkowicz, A.G.; Etzelmüller, B.; Smith, S.L. Characteristics of Discontinuous Permafrost Based on Ground Temperature Measurements and Electrical Resistivity Tomography, Southern Yukon, Canada. *Permafr. Periglac. Process.* **2011**, *22*, 320–342. [[CrossRef](#)]
58. Forte, E.; French, H.M.; Raffi, R.; Santin, I.; Guglielmin, M. Investigations of Polygonal Patterned Ground in Continuous Antarctic Permafrost by Means of Ground Penetrating Radar and Electrical Resistivity Tomography: Some Unexpected Correlations. *Permafr. Periglac. Process.* **2022**, *33*, 226–240. [[CrossRef](#)]
59. Gusmeroli, A.; Liu, L.; Schaefer, K.; Zhang, T.; Schaefer, T.; Grosse, G. Active Layer Stratigraphy and Organic Layer Thickness at a Thermokarst Site in Arctic Alaska Identified Using Ground Penetrating Radar. *Arct. Antarct. Alp. Res.* **2015**, *47*, 195–202. [[CrossRef](#)]
60. Moorman, B.J.; Robinson, S.D.; Burgess, M.M. Imaging Periglacial Conditions with Ground-penetrating Radar. *Permafr. Periglac. Process.* **2003**, *14*, 319–329. [[CrossRef](#)]
61. Onaca, A.; Ardelean, F.; Ardelean, A.; Magori, B.; Sirbu, F.; Voiculescu, M.; Gachev, E. Assessment of Permafrost Conditions in the Highest Mountains of the Balkan Peninsula. *CATENA* **2020**, *185*, 104288. [[CrossRef](#)]
62. Arcone, S.A.; Lawson, D.E.; Delaney, A.J.; Strasser, J.C.; Strasser, J.D. Ground-penetrating Radar Reflection Profiling of Groundwater and Bedrock in an Area of Discontinuous Permafrost. *Geophysics* **1998**, *63*, 1573–1584. [[CrossRef](#)]
63. Watanabe, T.; Matsuoka, N.; Christiansen, H.H. Ice- and Soil-Wedge Dynamics in the Kapp Linné Area, Svalbard, Investigated by Two- and Three-Dimensional GPR and Ground Thermal and Acceleration Regimes. *Permafr. Periglac. Process.* **2013**, *24*, 39–55. [[CrossRef](#)]

64. Leger, E.; Dafflon, B.; Soom, F.; Peterson, J.; Ulrich, C.; Hubbard, S. Quantification of Arctic Soil and Permafrost Properties Using Ground-Penetrating Radar and Electrical Resistivity Tomography Datasets. *IEEE J. Sel. Top. Appl. Earth Obs. Remote Sens.* **2017**, *10*, 4348–4359. [[CrossRef](#)]
65. Bode, J.; Moorman, B.; Stevens, C.; Solomon, S. Estimation of Ice Wedge Volume in the Big Lake Area, Mackenzie Delta, NWT, Canada. In Proceedings of the 9th International Conference on Permafrost, Fairbanks, AK, USA, 29 June–3 July 2008.
66. Yoshikawa, K.; Leuschen, C.; Ikeda, A.; Harada, K.; Gogineni, P.; Hoekstra, P.; Hinzman, L.; Sawada, Y.; Matsuoka, N. Comparison of Geophysical Investigations for Detection of Massive Ground Ice (Pingo Ice). *J. Geophys. Res. Planets* **2006**, *111*, 2005JE002573. [[CrossRef](#)]
67. Bouchard, F.; Francus, P.; Pienitz, R.; Laurion, I.; Feyte, S. Subarctic Thermokarst Ponds: Investigating Recent Landscape Evolution and Sediment Dynamics in Thawed Permafrost of Northern Québec (Canada). *Arct. Antarct. Alp. Res.* **2014**, *46*, 251–271. [[CrossRef](#)]
68. Anderson, D.; Ford, J.D.; Way, R.G. The Impacts of Climate and Social Changes on Cloudberry (Bakeapple) Picking: A Case Study from Southeastern Labrador. *Hum. Ecol.* **2018**, *46*, 849–863. [[CrossRef](#)] [[PubMed](#)]
69. Davis, E.; Trant, A.; Hermanutz, L.; Way, R.G.; Lewkowicz, A.G.; Siegwart Collier, L.; Cuerrier, A.; Whitaker, D. Plant–Environment Interactions in the Low Arctic Torngat Mountains of Labrador. *Ecosystems* **2021**, *24*, 1038–1058. [[CrossRef](#)]
70. Wang, Y.; Way, R.G.; Beer, J.; Forget, A.; Tutton, R.; Purcell, M.C. Significant Underestimation of Peatland Permafrost along the Labrador Sea Coastline in Northern Canada. *Cryosphere* **2023**, *17*, 63–78. [[CrossRef](#)]
71. Way, R.; Lewkowicz, A.; Wang, Y.; McCarney, P. Permafrost Investigations Below The Marine Limit At Nain, Nunatsiavut, Canada. In Proceedings of the Regional Conference on Permafrost 2021 and the 19th International Conference on Cold Regions Engineering, Reston, VA, USA, 24–29 October 2021. [[CrossRef](#)]
72. French, H.M. *The Periglacial Environment*, 4th ed.; Wiley, Blackwell: Hoboken, NJ, USA, 2017; ISBN 978-1-119-13281-3.
73. Connon, R.; Devoie, É.; Hayashi, M.; Veness, T.; Quinton, W. The Influence of Shallow Taliks on Permafrost Thaw and Active Layer Dynamics in Subarctic Canada. *J. Geophys. Res. Earth Surf.* **2018**, *123*, 281–297. [[CrossRef](#)]
74. Devoie, É.G.; Craig, J.R.; Dominico, M.; Carpino, O.; Connon, R.F.; Rudy, A.C.A.; Quinton, W.L. Mechanisms of Discontinuous Permafrost Thaw in Peatlands. *J. Geophys. Res. Earth Surf.* **2021**, *126*, e2021JF006204. [[CrossRef](#)]
75. Kasprzak, M. Seawater Intrusion on the Arctic Coast (Svalbard): The Concept of Onshore-Permafrost Wedge. *Geosciences* **2020**, *10*, 349. [[CrossRef](#)]
76. Dobiński, W.; Kasprzak, M. Permafrost Base Degradation: Characteristics and Unknown Thread With Specific Example From Hornsund, Svalbard. *Front. Earth Sci.* **2022**, *10*, 802157. [[CrossRef](#)]
77. Smith, S.L.; O’Neill, H.B.; Isaksen, K.; Noetzi, J.; Romanovsky, V.E. The Changing Thermal State of Permafrost. *Nat. Rev. Earth Environ.* **2022**, *3*, 10–23. [[CrossRef](#)]
78. Production de la 2e Approximation de la Carte de Pergélisol du Québec en Fonction des Paramètres Géomorphologiques, Écologiques, et des Processus Physiques Liés au Climat. Available online: <https://mffp.gouv.qc.ca/nos-publications/production-2e-approximation-carte-pergelisol-quebec/> (accessed on 14 December 2023).
79. Martin, L.; Nitzbon, J.; Aas, K.; Eitzelmüller, B.; Kristiansen, H.; Westermann, S. Stability Conditions of Peat Plateaus and Palsas in Northern Norway. *J. Geophys. Res. Earth Surf.* **2019**, *124*, 705–719. [[CrossRef](#)]
80. Shur, Y.L.; Jorgenson, M.T. Patterns of Permafrost Formation and Degradation in Relation to Climate and Ecosystems. *Permafr. Periglac. Process.* **2007**, *18*, 7–19. [[CrossRef](#)]
81. Spence, C.; Norris, M.; Bickerton, G.; Bonsal, B.R.; Brua, R.; Culp, J.M.; Dibike, Y.; Gruber, S.; Morse, P.D.; Peters, D.L.; et al. The Canadian Water Resource Vulnerability Index to Permafrost Thaw (CWRVI<sub>PT</sub>). *Arct. Sci.* **2020**, *6*, 437–462. [[CrossRef](#)]
82. Wright, S.N.; Thompson, L.M.; Olefeldt, D.; Connon, R.F.; Carpino, O.A.; Beel, C.R.; Quinton, W.L. Thaw-Induced Impacts on Land and Water in Discontinuous Permafrost: A Review of the Taiga Plains and Taiga Shield, Northwestern Canada. *Earth-Sci. Rev.* **2022**, *232*, 104104. [[CrossRef](#)]
83. Guimond, J.A.; Mohammed, A.A.; Walvoord, M.A.; Bense, V.F.; Kurylyk, B.L. Saltwater Intrusion Intensifies Coastal Permafrost Thaw. *Geophys. Res. Lett.* **2021**, *48*, e2021GL094776. [[CrossRef](#)]
84. Porada, P.; Ekici, A.; Beer, C. Effects of Bryophyte and Lichen Cover on Permafrost Soil Temperature at Large Scale. *Cryosphere* **2016**, *10*, 2291–2315. [[CrossRef](#)]
85. Tjellén, A.K.E.; Kristiansen, S.M.; Matthiesen, H.; Pedersen, O. Impact of Roots and Rhizomes on Wetland Archaeology: A Review. *Conserv. Manag. Archaeol. Sites* **2015**, *17*, 370–391. [[CrossRef](#)]
86. Dawson, T.; Hambly, J.; Kelley, A.; Lees, W.; Miller, S. Coastal Heritage, Global Climate Change, Public Engagement, and Citizen Science. *Proc. Natl. Acad. Sci. USA* **2020**, *117*, 8280–8286. [[CrossRef](#)]

**Disclaimer/Publisher’s Note:** The statements, opinions and data contained in all publications are solely those of the individual author(s) and contributor(s) and not of MDPI and/or the editor(s). MDPI and/or the editor(s) disclaim responsibility for any injury to people or property resulting from any ideas, methods, instructions or products referred to in the content.